Fault-Tolerant Control of Primary Permanent-Magnet Linear Motors With Single Phase Current Sensor for Subway Applications

Wei Wang, *Member, IEEE*, Yanan Feng, Yan Shi, Ming Cheng, *Fellow, IEEE*, Wei Hua, *Senior Member, IEEE*, and Zheng Wang, *Senior Member, IEEE*

***Abstract*—Because both magnets and windings can be mounted in the mover, the primary permanent-magnet linear motor (PPMLM) has a low-cost advantage for subway applications. In this paper, a fault-tolerant control (FTC) with single phase current sensor is proposed for PPMLM traction system in subway applications. In the proposed FTC, *d*- and *q*-axis currents are estimated from the reference synchronous currents and the surviving measured phase current. The estimation is robust since no machine parameters are required. In steady-state operation, the estimated current errors are half the actual ones. As a result, the current response is slowed but the current command can be achieved. However, the achievement of control target depends on the current tracking accuracy, which is enhanced by the voltage decoupler. Compared with existed FTC schemes, the proposed one is robust and has better transient-state performances. The effectiveness of the proposed FTC is verified by theoretical analysis and experimental results.**

***Index Terms*—Current estimation, fault-tolerance, primary permanent-magnet linear motor (PPMLM), single phase current sensor.**

I. Introduction

COMPARED with the rotational motor, the linear motor has several outstanding advantages for subway applications [1]–[5]. First, the linear motor can directly produce thrust force without the conversion from rotational motion to linear motion, and the thrust force does not depend on the friction between wheel and rail. Second, the linear motor has a smaller turning radius, a smaller cross-sectional area for the requirement of a tunnel, larger acceleration, and stronger climbing ability. Third,

Manuscript received November 26, 2018; revised January 13, 2019; accepted February 6, 2019. Date of publication February 13, 2019; date of current version August 29, 2019. This work was supported in part by the National Natural Science Foundation of China (Project: 51607038), in part by Jiangsu Natural Science Foundation of China (Project: BK20160673), in part by the Fundamental Research Funds for the Central Universities of China (Project: 2242017K41005), in part by ZhiShan Young Scholar Plan of Southeast University of China, and in part by Jiangsu Key Laboratory of Smart Grid Technology and Equipment of China. Recommended for publication by Associate Editor J. Hur. *(Corresponding author: Wei Wang.)*

The authors are with the School of Electrical Engineering, Southeast University, Nanjing 210096, China (e-mail:

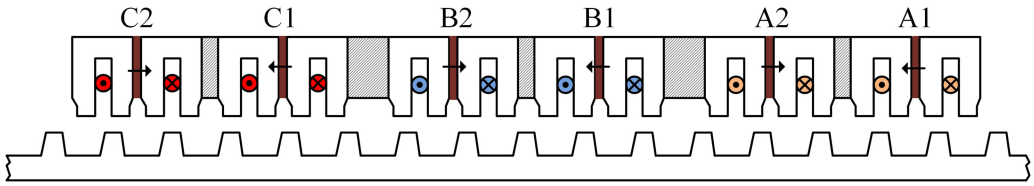

Fig. 1. Structure of the studied PPMLM.

their dependence on accurate motor models weakens system robustness. Therefore, another idea receives more attentions to adopt the dc-link current. It is known that the dc-link current can reflect one phase current if the voltage-source-inverter (VSI) is operated with one active voltage vector. Taking direct torque control (DTC) using a switching table as an example, only one phase current can be sensed by the dc-link current sensor in one switching period. The DTC using single dc-link current sensor in [26] first predicts the phase currents by an IM model and then adjusts the predicted phase currents with the measured dc-link current. However, this scheme requires an accurate IM model and more motor parameters in addition to the stator resistance of the IMs, which also degrades reliability. In [27], a fast switching DTC is proposed, in which two adjacent voltage vectors are synthesized as a new complex voltage vector, and they are outputted according to the different phase mode. Fortunately, the two adjacent active voltage vectors reflect two different phase currents. As a result, all phase currents can be reconstructed in two adjacent switching periods. This method inherits the advantages of the conventional DTC. In fact, the idea in [27] is very similar to the space-vector-pulsewidth-modulation (SVPWM), i.e., the reference voltage vector of SVPWM-VSI is usually synthesized by two adjacent active voltage vectors in one switching period. In other words, three-phase currents can be reconstructed in one switching period by single dc-link current sensor for SVPWM-VSI if their summation is zero. According to this idea, many control schemes using a single dc-link current sensor have been presented [28]–[33]. However, these methods have the blind zone for current reconstruction. If the duration of the active voltage vector is not long enough to ensure a proper sampling of the dc-link current, the phase current reconstruction will fail. Hence, nearly all SVPWM-based methods must overcome the blind zone and the original reference voltage vector may be modified.

As it is well known, the dc-link current sensor is not always mounted in motor drive systems. In such a situation, once one phase current sensor fails, all the FTC methods based on the dc-link current sensor will be invalid. However, very few papers have focused on this topic [34]–[36]. In [34], the actual d- and q-axis currents are estimated from the reference ones and the only surviving measured phase current. During the estimation, no additional IM parameters are required. However, only the steady-state performances are provided. In [35] and [36], two FTCs are proposed for IM drives against phase current sensor failures, in which the α- and β-axis currents are estimated by IM model. Due to the existence of the IM model, the accuracy of estimated currents will be affected by IM parameters.

Unfortunately, to the best of authors' knowledge, no existing literature has discussed the FTC of PPMLM using single-phase current sensor. The target of this paper is to propose a novel FTC for PPMLM using single-phase current sensor, which can be treated as the FTC of the axle-control PPMLM traction system proposed in [37]. Compared with existed FTCs using single phase current sensor [34]–[36], the proposed FTC performs better transient-state response but requires no motor parameters for current estimation, which is the main contribution of this paper. This paper is organized as follows. The studied PPMLM traction system is defined in Section II. The proposed FTC using single phase current sensor is presented in Section III, and its performances are analyzed in Section IV. Some experiments are carried out to verify the effectiveness of the proposed FTC in Section V. Finally, some conclusions are drawn in Section VI.

II. Studied PPMLM Traction System

A. System Topology

The structure of the studied PPMLM is shown in Fig. 1. Both magnets and armature windings are mounted in movers. The secondary is mounted in the rail. The topology of the studied axle-control PPMLM traction system is illustrated in Fig. 2, which contains four three-phase movers (Mover 1–Mover 4), and each three-leg VSI just feeds single three-phase mover. All VSIs are supplied by the contacting grid. In this paper, VSI 1 and Mover 1 are selected as examples to explain the proposed FTC. The phase windings of Mover 1 are defined as phase-A, phase-B, and phase-C, respectively. The corresponding phase currents are defined as i_a, i_b, and i_c, respectively. Two current sensors are employed to sense i_a and i_b.

In this paper, the fault state of the PPMLM drive, F_x ($x = a,\ b$), is defined as follows.

1) $F_x = 0$: phase-*X* current sensor is healthy.
2) $F_x = 1$: phase-*X* current sensor is faulty.

According to the value combination of F_a and F_b, the system operation can be divided into three different situations as follows.

1) Normal operation: $F_a = 0$ and $F_b = 0$.
2) Fault-A operation: $F_a = 1$ and $F_b = 0$.
3) Fault-B operation: $F_a = 0$ and $F_b = 1$.

B. Mathematical Model of PPMLM

The d- and q-axis of PPMLM are defined in Fig. 3. The d-axis is in the center of stator teeth, where the PM flux linkage is maximum. The q-axis is the primary position with the minimum (zero) PM flux linkage. The relative displacement between d- and q-axis is $\tau_s/4$, where τ_s is the stator pole pitch. When the positive PM flux linkage passing through phase-A winding

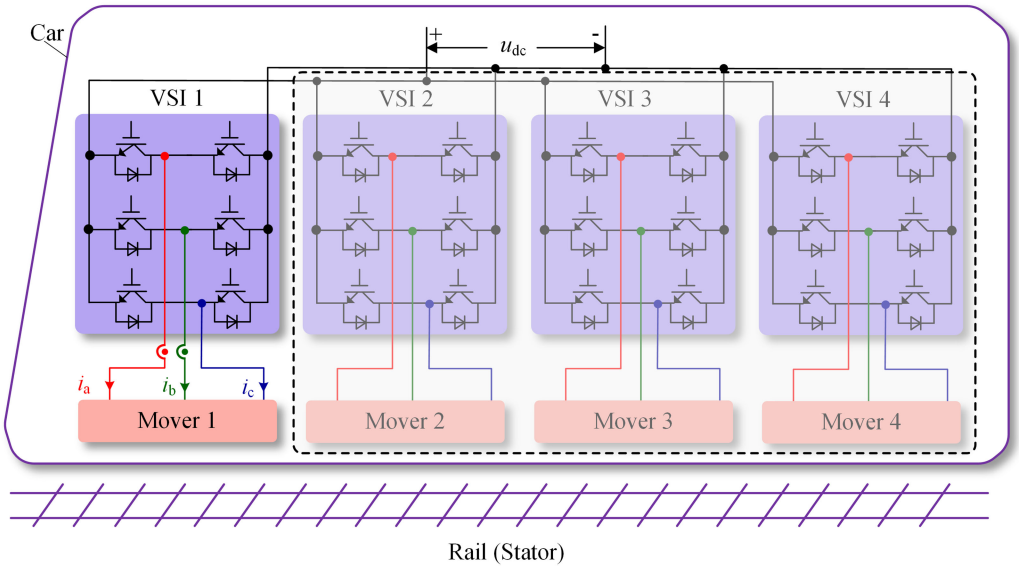

Fig. 2. Topology of the studied PPMLM traction system.

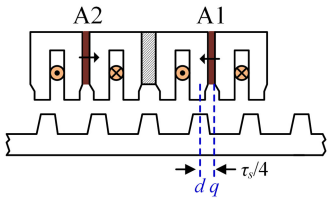

Fig. 3. Definition of d- and q-axis for PPMLM.

is maximum, the corresponding primary position is defined as zero, as shown in Fig. 3.

Based on the above-mentioned definition, the dynamic voltage equations can be expressed as

$$\begin{cases} u_d = R_s i_d + \frac{d\psi_d}{dt} - \omega_e \psi_q \\ u_q = R_s i_q + \frac{d\psi_q}{dt} + \omega_e \psi_d \end{cases} \tag{1}$$

with

$$\begin{cases} \psi_d = \psi_f + L_d i_d + L_{dq} i_q \\ \psi_q = L_q i_q + L_{qd} i_d \end{cases} \tag{2}$$

$$\begin{cases} L_d = L_{\mathrm{DC}} + L_m \cos(3\theta_e)/2 \\ L_q = L_{\mathrm{DC}} - L_m \cos(3\theta_e)/2 \\ L_{dq} = L_{qd} = L_m \cos(3\theta_e)/2 = 0 \end{cases} \tag{3}$$

where θ_e is electrical degree of the primary position; $\omega_e = 2\pi\nu_m/\tau_s$ is the electrical angular speed; ν_m is the mover speed; ψ_f is the peak value of the PM flux linkage; L_d and L_q are the d- and q-axis stator inductances, respectively; i_d and i_q are the d- and q-axis stator currents, respectively; u_d and u_q are the d- and q-axis stator voltages, respectively; ψ_d and ψ_q are the d- and q-axis stator flux linkages, respectively; R_s is the stator resistance; L_{DC} and L_m are the dc component and the fundamental component amplitude of self-inductance, respectively. Because L_m is very small, it is neglected in this paper, and $L_d = L_q = L_{\mathrm{DC}}$. In this paper, L_{DC} is redefined as the stator inductance L_s.

Substituting (2) and (3) into (1) gives

$$\begin{cases} u_d = R_s i_d + L_s \frac{di_d}{dt} - \omega_e L_s i_q \\ u_q = R_s i_q + L_s \frac{di_q}{dt} + \omega_e (L_s i_d + \psi_f). \end{cases} \tag{4}$$

In steady-state operation, (4) can be simplified as

$$\begin{cases} u_d = R_s i_d - \omega_e L_s i_q \\ u_q = R_s i_q + \omega_e (L_s i_d + \psi_f). \end{cases} \tag{5}$$

According to (5), the electromagnetic thrust force is deduced as

$$F_e = \frac{3\pi\psi_f i_q}{\tau_s}. \tag{6}$$

III. Proposed FTC

In this section, the proposed FTC is explained in detail. The control block diagram of the proposed FTC is illustrated in Fig. 4, which includes one speed regulator, two current regulators, one voltage decoupler, one SVPWM module, one current estimator, a-b/α-β transformation module, one fault diagnosis module, one current optimizer, and one synchronous current generator. All these modules will be described in this section. To clarify the analysis, the space distribution of the three-phase static coordinate system (a-b-c), the two-phase static coordinate system (α-β), and the two-phase synchronous coordinate system (d-q) is illustrated in Fig. 5. In α-β coordinate system, α-axis lags 90° behind β-axis but is ahead of phase-A with the angle γ. The value of γ is varied in different situations: 0 in normal and Fault-B operation, and 120° in Fault-A operation.

A. Speed Regulator and Current Regulators

These three regulators are proportional-integral type. The speed regulator outputs the reference q-axis current i_q^* by

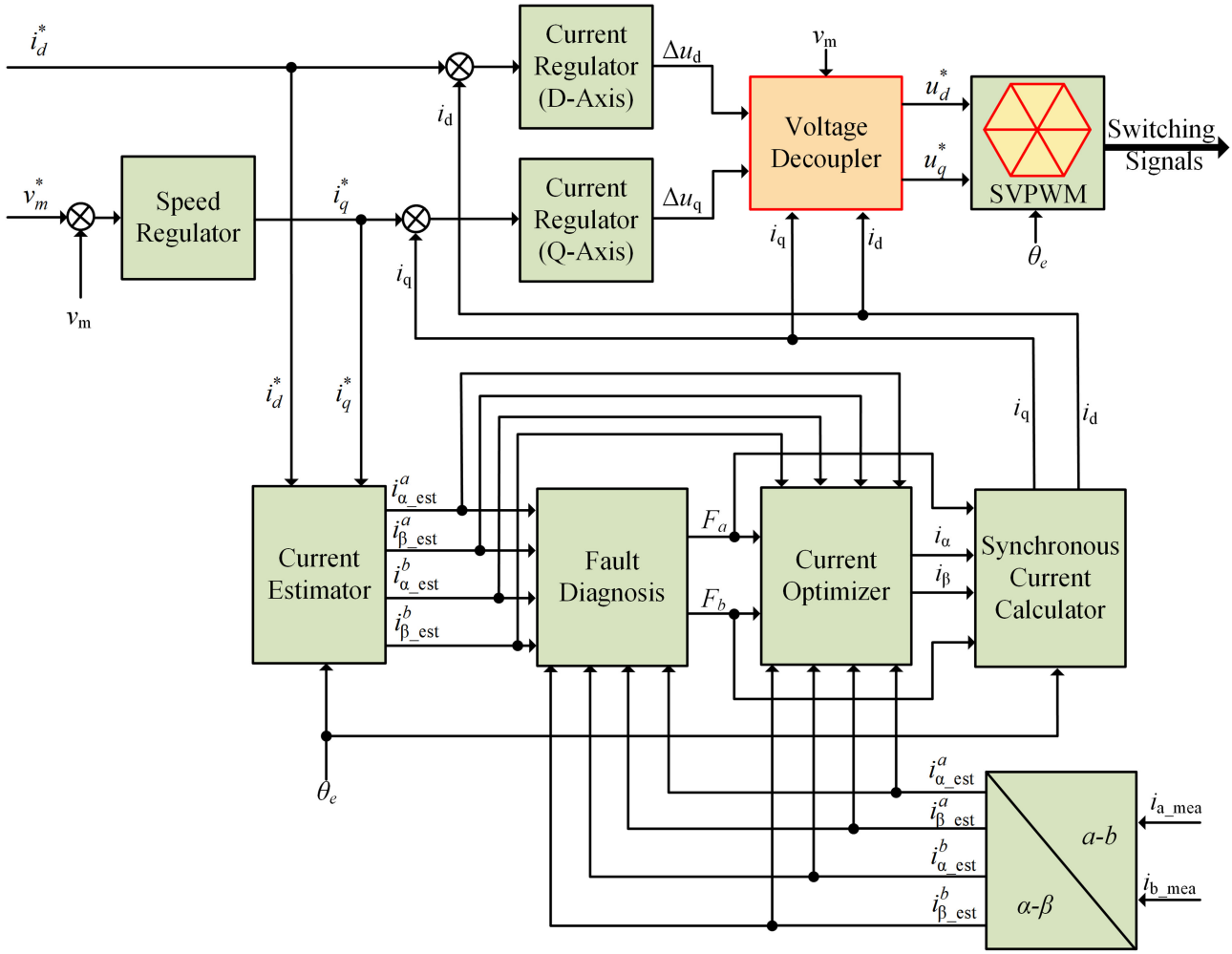

Fig. 4. Control block diagram of the proposed FTC.

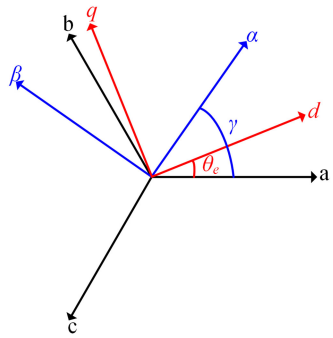

Fig. 5. Space distribution of three different coordinate systems.

comparing the reference v_m^* and actual mover speed v_m. By comparing the reference i_d^* and actual d-axis current i_d, the d-axis voltage increment Δu_d can be obtained from the d-axis current regulator. Similarly, the q-axis voltage increment Δu_q can be obtained from the q-axis current regulator by comparing the reference i_q^* and actual q-axis current i_q. However, no matter in Fault-A situation or Fault-B situation, the actual d-axis current i_d and the actual q-axis current i_q cannot be directly measured since one phase current sensor has been invalid, which is the key challenge of the proposed FTC.

B. Voltage Decoupler

In this module, the d- and q-axis are decoupled by compensating the voltage drop of the stator resistance and the back electromotive force to fasten the current response, which will be deeply analyzed in next section. The working principles are derived from (4) as follows:

$$\begin{cases} u_d^* = R_s i_d + \Delta u_d - 2\pi v_m L_s i_q/\tau_s \\ u_q^* = R_s i_q + \Delta u_q + 2\pi v_m (L_s i_d + \psi_f)/\tau_s \end{cases} \tag{7}$$

where u_d^* and u_q^* are reference d- and q-axis stator voltages, respectively.

C. Space-Vector-Pulsewidth-Modulation

The SVPWM module is employed to generate switching signals according to the SVPWM theory, which has been reported in a lot of papers [38] and will not be discussed in this paper.

D. Current Estimator

In the proposed FTC, it is assumed that the reference currents can be well followed. At least, the errors between the reference and actual currents should be small. Based on this pre-condition, α- and β- axis currents can be estimated by

$$\begin{bmatrix} i^x_{\alpha\_\mathrm{est}} \\ i^x_{\beta\_\mathrm{est}} \end{bmatrix} = \begin{bmatrix} \cos(\theta_e-\gamma) & -\sin(\theta_e-\gamma) \\ \sin(\theta_e-\gamma) & \cos(\theta_e-\gamma) \end{bmatrix} \begin{bmatrix} i^*_d \\ i^*_q \end{bmatrix}, x=a,b \tag{8}$$

where $i^a_{\alpha\_\mathrm{est}}$ and $i^a_{\beta\_\mathrm{est}}$ are estimated α- and β-axis currents in normal or Fault-B operation, respectively; $i^b_{\alpha\_\mathrm{est}}$ and $i^b_{\beta\_\mathrm{est}}$ are estimated α- and β-axis currents in Fault-A operation, respectively.

E. a-b/α-β Coordinate Transformation

According to Fig. 5, this module converts measured phase currents into measured α- and β-axis currents as follows:

$$\begin{bmatrix} i^x_{\alpha\_\mathrm{mea}} \\ i^x_{\beta\_\mathrm{mea}} \end{bmatrix} = \frac{2\sqrt{3}}{3} \begin{bmatrix} \cos(30^\circ-\gamma) & \sin\gamma \\ \sin(30^\circ-\gamma) & \cos\gamma \end{bmatrix} \begin{bmatrix} i_{a\_\mathrm{mea}} \\ i_{b\_\mathrm{mea}} \end{bmatrix}, x=a,b \tag{9}$$

where $i^a_{\alpha\_\mathrm{mea}}$ and $i^a_{\beta\_\mathrm{mea}}$ are measured α- and β-axis currents in normal or Fault-B operation; $i^b_{\alpha\_\mathrm{mea}}$ and $i^b_{\beta\_\mathrm{mea}}$ are measured α- and β-axis currents in Fault-A operation.

F. Fault Diagnosis

In this module, the current sensor faults can be detected by determining the value of the fault state. In normal operation, the differences between $i^x_{\alpha\_\mathrm{mea}}$ and $i^x_{\alpha\_\mathrm{est}}$ are very small. Once one current sensor fails, the corresponding α-axis current difference will become large immediately. According to this fact, the current sensor fault can be detected. The fault state F_x can be determined by

$$F_x = \begin{cases} 1, |i^x_{\alpha\_\mathrm{est}} - i^x_{\alpha\_\mathrm{mea}}| \geq I_\mathrm{th} \\ 0, |i^x_{\alpha\_\mathrm{est}} - i^x_{\alpha\_\mathrm{mea}}| < I_\mathrm{th} \end{cases}, x=a,b \tag{10}$$

where I_th is the threshold value of the fault diagnosis module. It is a positive constant. As is known, the current tracking error between the estimated and measured α-axis current exists. Therefore, twice of the maximum current tracking error in steady-state operation is set as the value of I_th in this paper, which may be not appropriate. In such situation, the implementation of the proposed FTC may be delayed. In the worst situation, the post-fault operation of the PPMLM may be broken. However, the key point of this paper is to propose a FTC instead of fault diagnosis, and this module just provides a simple fault diagnosis method as an example. A better fault diagnosis method will be investigated in future.

G. Current Optimizer

In normal operation, $i^a_{\alpha\_\mathrm{mea}}$ and $i^a_{\beta\_\mathrm{mea}}$ can be directly measured by two healthy current sensors. Hence, the final α- and β-axis (i_α, i_β) can be determined by

$$\begin{cases} i_\alpha = i^a_{\alpha\_\mathrm{mea}} \\ i_\beta = i^a_{\beta\_\mathrm{mea}}. \end{cases} \tag{11a}$$

In Fault-A operation, only phase-B current can be directly measured. In this situation, the estimated β-axis current $i^b_{\beta\_\mathrm{est}}$ is treated as the actual current to maintain the continuous operation of the PPMLM. Hence, the final α- and β-axis (i_α, i_β) can be determined by

$$\begin{cases} i_\alpha = i^b_{\alpha\_\mathrm{mea}} \\ i_\beta = i^b_{\beta\_\mathrm{est}}. \end{cases} \tag{11b}$$

In Fault-B operation, only phase-A current can be directly measured. Similarly, the final α- and β-axis (i_α, i_β) can be determined by

$$\begin{cases} i_\alpha = i^a_{\alpha\_\mathrm{mea}} \\ i_\beta = i^a_{\beta\_\mathrm{est}}. \end{cases} \tag{11c}$$

Considering (11a)–(11c) and the fault states (F_a, F_b), the final α- and β-axis (i_α, i_β) can be determined by a common expression as follows

$$\begin{cases} i_\alpha = (1-F_a) i^a_{\alpha\_\mathrm{mea}} + F_a i^b_{\alpha\_\mathrm{mea}} \\ i_\beta = (1-F_a)(1-F_b) i^a_{\beta\_\mathrm{mea}} + F_a i^b_{\beta\_\mathrm{est}} + F_b i^a_{\beta\_\mathrm{est}}. \end{cases} \tag{11d}$$

H. Synchronous Current Generator

This module is employed to convert (i_α, i_β) into synchronous currents (i_d, i_q) by

$$\begin{bmatrix} i_d \\ i_q \end{bmatrix} = \begin{bmatrix} \cos(\gamma-\theta_e) & -\sin(\gamma-\theta_e) \\ \sin(\gamma-\theta_e) & \cos(\gamma-\theta_e) \end{bmatrix} \begin{bmatrix} i_\alpha \\ i_\beta \end{bmatrix}. \tag{12}$$

IV. Performance Analysis

The performances of the proposed FTC is analyzed in this section. In normal operation, the reference currents can be well followed since the optimal control commands can be generated by comparing the reference and measured currents. However, the actual *d*- and *q*-axis currents cannot be obtained in post-fault operation. To maintain the continuous operation of the PPMLM, the *d*- and *q*-axis currents are estimated from the reference synchronous currents and the surviving measured phase currents. It is wondered why the actual synchronous currents can be controlled by the estimated ones. The reasons will be provided in this section. In fact, the errors between the estimated and actual synchronous currents cannot be totally eliminated, especially in transient-state operation. If the errors are not strictly limited, the performances of the two current regulators will be affected. One challenge of the proposed FTC is to restrain the current tracking errors, especially in the transient-state situation.

A. Effectiveness in Steady-State Operation

It is assumed that the PPMLM has come into Fault-B operation. According to the current optimizer, the measured α-axis

current and the estimated β-axis current are adopted as follows:

$$\begin{cases} i_\alpha = i^a_{\alpha\_\mathrm{mea}} \\ i_\beta = i^a_{\beta\_\mathrm{est}}. \end{cases} \tag{13}$$

According to (8), $i^a_{\alpha\_\mathrm{mea}}$ and $i^a_{\beta\_\mathrm{est}}$ can be represented as

$$\begin{cases} i^b_{\alpha\_\mathrm{mea}} = i_{d\_\mathrm{act}} \cos\theta_e - i_{q\_\mathrm{act}} \sin\theta_e \\ i^b_{\beta\_\mathrm{est}} = i^*_d \sin\theta_e + i^*_q \cos\theta_e \end{cases} \tag{14}$$

where i_{d_act} and i_{q_act} are actual d- and q-axis currents, respectively.

Substituting (13) and (14) into (12) gives

$$\begin{cases} \Delta i_{d\_\mathrm{est}} = \frac{1}{2}\Delta i_{d\_\mathrm{act}}(1+\cos 2\theta_e) - \frac{1}{2}\Delta i_{q\_\mathrm{act}} \sin 2\theta_e \\ \Delta i_{q\_\mathrm{est}} = \frac{1}{2}\Delta i_{q\_\mathrm{act}}(1-\cos 2\theta_e) - \frac{1}{2}\Delta i_{d\_\mathrm{act}} \sin 2\theta_e \end{cases} \tag{15}$$

with

$$\begin{cases} \Delta i_{d\_\mathrm{est}} = i^*_d - i_{d\_\mathrm{est}}, \Delta i_{q\_\mathrm{est}} = i^*_q - i_{q\_\mathrm{est}} \\ \Delta i_{d\_\mathrm{act}} = i^*_d - i_{d\_\mathrm{act}}, \Delta i_{q\_\mathrm{act}} = i^*_q - i_{q\_\mathrm{act}} \end{cases}$$

where i_{d_est} and i_{q_est} are the estimated d- and q-axis currents, respectively; $\Delta i_{d\_\mathrm{est}}$ is the error between the reference and estimated d-axis currents; $\Delta i_{q\_\mathrm{est}}$ is the error between the reference and estimated q-axis currents; $\Delta i_{d\_\mathrm{act}}$ is the error between the reference and actual d-axis current; $\Delta i_{q\_\mathrm{act}}$ is the error between the reference and actual q-axis current.

In high-speed steady-state operation, the current period is significantly shorter than the mechanical time constant of the studied PPMLM. Therefore, the periodic influences of the synchronous currents to the mover speed can be ignored. As a result, (15) can be simplified as

$$\begin{cases} \Delta i_{d\_\mathrm{est}} = \frac{1}{2}\Delta i_{d\_\mathrm{act}} \\ \Delta i_{q\_\mathrm{est}} = \frac{1}{2}\Delta i_{q\_\mathrm{act}}. \end{cases} \tag{16}$$

As it is found in (16), the estimated current errors are half the actual ones in steady-state post-fault operation. Hence, the response of the current command will be slowed. However, the control targets can be achieved since the direction of the current change is not affected.

When the speed is so low that the current period is close the mechanical time constant of the studied PPMLM, the periodic influences of the synchronous currents to the mover speed cannot be ignored. However, the average mover speed can remain.

B. Limit the Current Tracking Errors

Because the reference currents are treated as the actual currents in post-fault operation, the current tracking accuracy is very important for the proposed FTC. As it is well known, the current tracking error can be very small during steady-state operation. However, the current tracking error may be significantly increased in the transient-state operation. If the increased current tracking error cannot be reduced as soon as possible, the proposed FTC may fail. According to (4), d- and q-axis currents are coupled together. Once the q-axis current i_q is changed, the d-axis current i_d will be affected if the d-axis voltage cannot be quickly regulated. The q-axis current also can be affected by d-axis current if the voltage decoupler is not employed. According to (7), the resistance voltage drops and the back electromotive forces are compensated. The outputs of two current regulators directly focus on the corresponding stator inductances. As a result, the d- and q-axis coupling effects can be significantly weakened. It seems that the connection between d- and q-axis currents has been broken, and they can be independently controlled by their own regulators. Hence, the current response can be fastened, which will increase the current tracking accuracy.

Based on the above-mentioned analysis, the proposed FTC is effective in no matter steady-state or transient-state operations.

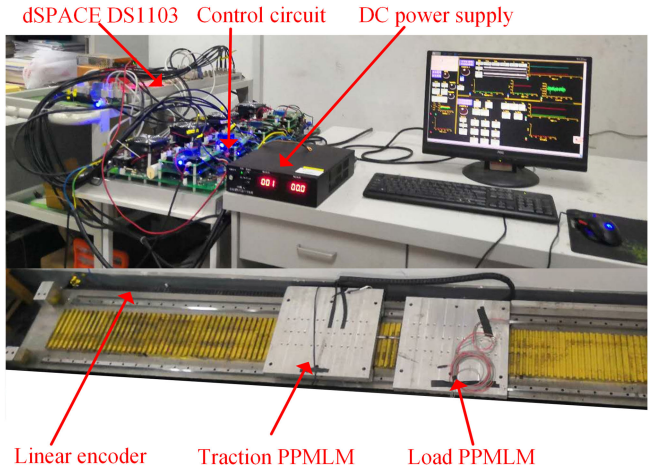

Fig. 6. Experiment platform.

V. Experimental Validation

To validate the effectiveness of the proposed FTC, two same PPMLMs are manufactured and an experiment platform is developed, as shown in Fig. 6. The two PPMLMs with a linear encoder are connected together and their parameters are listed in Table I. One PPMLM plays the role of the studied traction motor and the other one is treated as the load motor. The load is realized by the close-loop thrust force control of the load PPMLM. Due to the expensive cost, the power level of the studied PPMLM is small. The dc-link voltage is 150 V. The control program is implemented in a dSPACE DS1103 controller. The inputs for the dSPACE DS1103 controller are the measured phase currents and dc-link voltage, and the feedback signal of the linear encoder. The switch states for the VSIs are generated by the dSPACE DS1103 controller. A personal computer is employed for editing the control program and commanding the dSPACE DS1103 controller. The sampling frequency is 25 kHz. To emphasize the effect of the voltage decoupler, the proposed FTC is compared with an existing one, which does not contain the voltage decoupler [34]. To simplify the description, the proposed FTC is defined as FTC-I whereas the existing one proposed in [34] is defined as FTC-II. Several experiments are carried out and the experimental results are compared.

TABLE I
PARAMETERS OF PPMLM

Parameter	Value
Mover width, w_m (mm)	160
Mover pole pitch, τ_m (mm)	26
Stator pole pitch, τ_s (mm)	24
Mover tooth width, w_{mt} (mm)	6.5
Mover slot mouth width w_{msm}(mm)	6.5
Mover slot width w_{ms} (mm)	6.5
Slot width (Under PM), w_{ms} (mm)	6.5
Mover height, h_m (mm)	35
Mover yoke height, h_{my} (mm)	10
Magnet height, h_{pm} (mm)	0.9*h_m
Magnet width, w_{pm} (mm)	5
Air gap length, g (mm)	2
Stator tooth width, w_{st} (mm)	1.6*τ_m/4
Stator teeth yoke width, w_{sty} (mm)	2*τ_m/4
Stator tooth height, h_{st} (mm)	10
Stator yoke height, h_{sy} (mm)	13
Stator height, h_s (mm)	23
Coil spacing, λ_1 (mm)	(2+1/2)*τ_s
Phase spacing, λ_2 (mm)	(5+1/3)*τ_s
Number of turns per coil, N_{coil}	114
Phase resistance (Ω), R_s	3
Stack factor	0.95
Rated current I_{rms} (A)	3

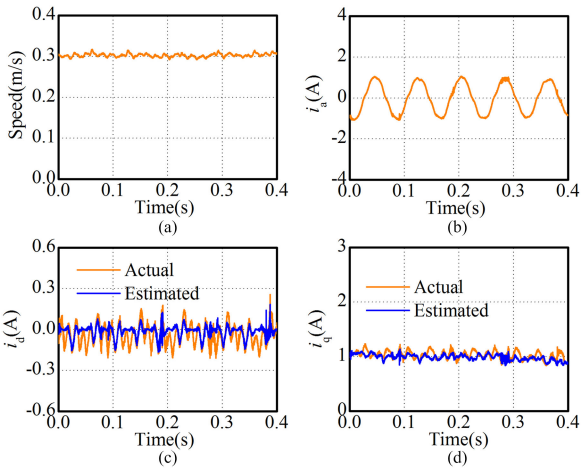

Fig. 7. Steady-state waveforms of FTC-I with 50 N load. (a) Speed. (b) Measured current of phase-A. (c) Estimated and actual d-axis currents. (d) Estimated and actual q-axis currents.

A. Experiment 1: Steady-State Performances With 50 N Load

This experiment is to test the performances of both FTCs in the steady-state operation with 50 N load. The speed command is 0.3 m/s and the studied PPMLM works in Fault-B operation. The experimental results are illustrated in Figs. 7 and 8. It can be found that the studied PPMLM can well follow the speed command by using FTC-I or FTC-II. Besides, the d- and q-axis current commands also can be well followed.

B. Experiment 2: Steady-State Performances With 100 N Load

This experiment is to test the performances of both FTC schemes in steady-state operation with 100 N·m. The other experimental conditions are as same as those in Experiment 1.

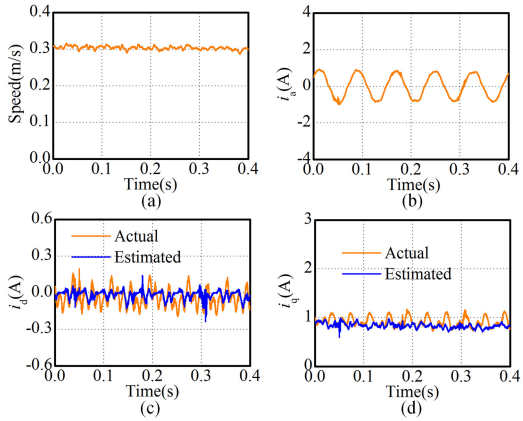

Fig. 8. Steady-state waveforms of FTC-II with 50 N load. (a) Speed. (b) Measured current of phase-A. (c) Estimated and actual d-axis currents. (d) Estimated and actual q-axis currents.

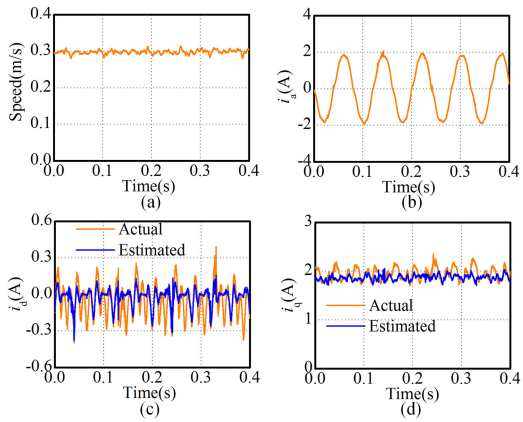

Fig. 9. Steady-state waveforms of FTC-I with 100 N load. (a) Speed. (b) Actual current of phase-A. (c) Estimated and actual d-axis currents. (d) Estimated and actual q-axis currents.

The experimental results are illustrated in Figs. 9 and 10. It can be found that both FTC-I and FTC-II have similar steady-state performances. Compared with Experiment 1, the current ripples become larger in Experiment 2.

C. Experiment 3: Thrust Response

This experiment is to test the thrust response of both FTC schemes. In this experiment, the thrust force is commanded to change from 200 N to −200 N, and then return to 200 N. During this transient-state procedure, the speed command remains 0.3 m/s unchanged. The experimental results are illustrated in Fig. 11. It can be found that the thrust response ability of FTC-I is significantly better than that of FTC-II.

D. Experiment 4: Speed Response

In this experiment, the speed is increased from 0.3 to 0.6 m/s, and then decreased to 0.3 m/s. The experimental results of FTC-I and FTC-II are illustrated in Figs. 12 and 13, respectively. It also can be found that FTC-I has better speed response performances than those of FTC-II.

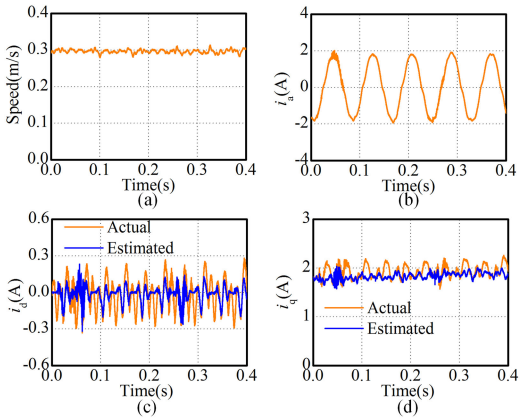

Fig. 10. Steady-state waveforms of FTC-II with 100 N load. (a) Speed. (b) Measured current of phase-A. (c) Estimated and actual *d*-axis currents. (d) Estimated and actual *q*-axis currents.

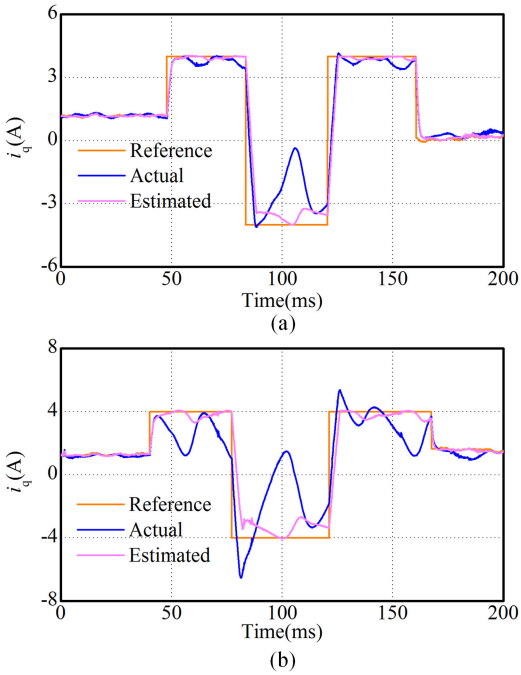

Fig. 11. Thrust response. (a) FTC-I. (b) FTC-II.

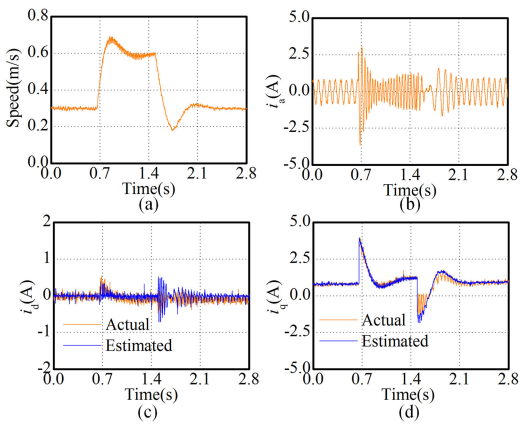

Fig. 12. Speed transient performances of FTC-I. (a) Speed. (b) Measured current of phase-A. (c) Estimated and actual *d*-axis currents. (d) Estimated and actual *q*-axis currents.

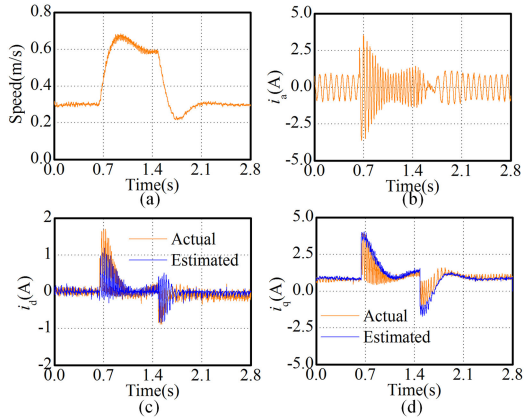

Fig. 13. Speed transient performances of FTC-II. (a) Speed. (b) Measured current of phase-A. (c) Estimated and actual *d*-axis currents. (d) Estimated and actual *q*-axis currents.

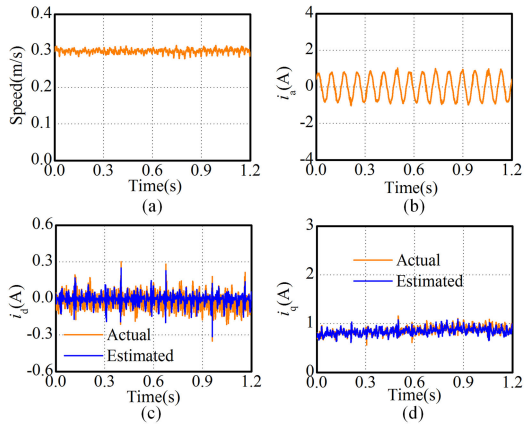

Fig. 14. Fault switching performances of FTC-I. (a) Speed. (b) Actual current of phase-A. (c) Estimated and actual *d*-axis currents. (d) Estimated and actual *q*-axis currents.

E. Experiment 5: Fault Switching

In this experiment, the studied PPMLM is switched from normal operation to Fault-B operation at $t = 0.5$ s. The experimental results of the switching procedure are illustrated in Figs. 14 and 15. The copper losses in normal operation using FTC-I and FTC-II are 2.98 W and 3.00 W, respectively. Those values in fault-tolerant operation are 3.70 W and 3.73 W, respectively. It can be found that FTC-I and FTC-II have similar steady-state performances no matter in normal or post-fault operations. However, the copper loss in fault-tolerant operation is increased by 24%, compared with that in normal operation. The reason is that the current tracking error cannot be reduced as soon as possible in fault-tolerant operation since one phase current information has been lost. As a result, the efficiency and power density in fault-tolerant operation are also lower than those in normal operation, as listed in Table II.

F. Experiment 6: Full-Speed Operation

In this experiment, the studied PPMLM works in Fault-B operation. The speed is increased from 0 to 0.3 m/s.

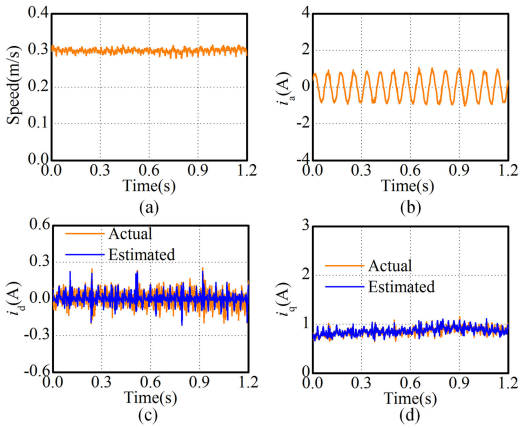

Fig. 15. Fault switching performances of FTC-II. (a) Speed. (b) Actual current of phase-A. (c) Estimated and actual *d*-axis currents. (d) Estimated and actual *q*-axis currents.

TABLE II
PERFORMANCE COMPARISONS

	Normal operation	Fault-tolerant operation
Efficiency	Higher	Lower
Power density	Higher	Lower

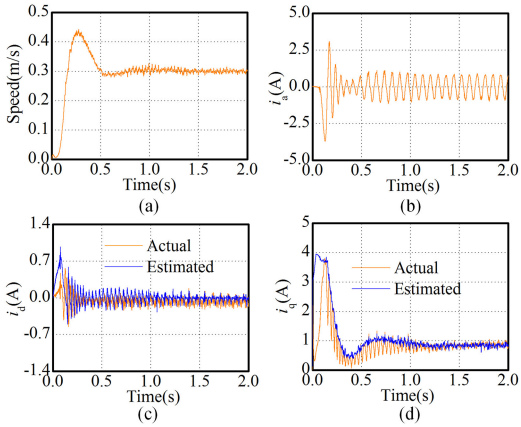

Fig. 16. Full-speed operation performances of FTC-I. (a) Speed. (b) Measured current of phase-A. (c) Estimated and actual *d*-axis currents. (d) Estimated and actual *q*-axis currents.

This control target can be realized by using FTC-I, and the experimental results are illustrated in Fig. 16. It can be found in Fig. 16(a) that the speed overshoot is significant. The reason is that *q*-axis current error is large at the start-up phase, as shown in Fig. 16(d). However, the studied PPMLM cannot be started by using FTC-II. Therefore, the experimental results are not provided here.

VI. CONCLUSION

In this paper, an FTC is proposed for the PPMLM traction system with single phase current sensor in subway applications. In the proposed FTC, synchronous currents are estimated from the reference ones and the surviving measured phase current. The estimation is robustness since no machine parameters are required. The effectiveness of the estimation is analyzed in theory. The voltage decoupler module is first introduced in such FTCs with single phase current sensor, which can fasten the current response. Compared with existed FTC schemes, the proposed one is robustness and has better transient-state performances. Even though the proposed FTC is proposed for PPMLM, it can be extended to the other three-phase electrical machines.

APPENDIX

The derivation process of (9) is provided in this section. According to Fig. 5, α- and β-axis currents can be determined by three phase currents as follows:

$$\begin{cases} i_\alpha^x = (2/3)[i_a \cos\gamma + i_b \cos(\gamma - 120^\circ) \\ \qquad +i_c \cos(\gamma + 120^\circ)] \\ i_\beta^x = -(2/3)[i_a \sin\gamma + i_b \sin(\gamma - 120^\circ) \\ \qquad +i_c \sin(\gamma + 120^\circ)] \end{cases}, x = a, b. \quad \text{(A-1)}$$

Because the summation of three-phase currents is zero, (A-1) can be rewritten by replacing i_c with $-(i_a + i_b)$ as follows:

$$\begin{cases} i_\alpha^x = (2/3)[i_a \cos\gamma + i_b \cos(\gamma - 120^\circ) \\ \qquad -(i_a + i_b) \cos(\gamma + 120^\circ)] \\ i_\beta^x = -(2/3)[i_a \sin\gamma + i_b \sin(\gamma - 120^\circ) \\ \qquad -(i_a + i_b) \sin(\gamma + 120^\circ)] \end{cases}, x = a, b. \quad \text{(A-2)}$$

(A-2) can be simplified as

$$\begin{bmatrix} i_\alpha^x \\ i_\beta^x \end{bmatrix} = \frac{2\sqrt{3}}{3} \begin{bmatrix} \cos(30^\circ - \gamma) & \sin\gamma \\ \sin(30^\circ - \gamma) & \cos\gamma \end{bmatrix} \begin{bmatrix} i_a \\ i_b \end{bmatrix}, x = a, b. \quad \text{(A-3)}$$

Since the currents of phase-A and phase-B can be measured by current sensors, (A-3) can be rewritten as (9).

REFERENCES

[1] J. Q. Li, W. L. Li, G. Q. Deng, and Z. Ming, "Continuous-behavior and discrete-time combined control for linear induction motor-based urban rail transit," *IEEE Trans. Magn.*, vol. 52, no. 7, pp. 1–4, Jul. 2016.
[2] W. Xu, J. G. Zhu, Y. Zhang, Y. Li, Y. Wang, and Y. Guo, "An improved equivalent circuit model of a single-sided linear induction motor," *IEEE Trans. Veh. Technol.*, vol. 59, no. 5, pp. 2277–2289, Jun. 2010.
[3] G. Lv, D. Zeng, T. Zhou, and Z. Liu, "Investigation of forces and secondary losses in linear induction motor with the solid and laminated back iron secondary for metro," *IEEE Trans. Ind. Electron.*, vol. 64, no. 6, pp. 4382–4390, Jun. 2017.
[4] R. Thornton, M. T. Thompson, B. M. Perreault, and J. Fang, "Linear motor powered transportation," *Proc. IEEE*, vol. 97, no. 11, pp. 1754–1757, Nov. 2009.
[5] J. Song, F. Dong, J. Zhao, S. Lu, S. Dou, and H. Wang, "Optimal design of permanent magnet linear synchronous motors based on Taguchi method," *IET Elect. Power Appl.*, vol. 11, no. 1, pp. 41–48, Jan. 2017.
[6] R. Hellinger and P. Mnich, "Linear motor-powered transportation: History, present status, and future outlook," *Proc. IEEE*, vol. 97, no. 11, pp. 1892–1900, Nov. 2009.
[7] G. Lv, T. Zhou, D. Zeng, and Z. Liu, "Design of ladder-slit secondaries and performance improvement of linear induction motors for urban rail transit," *IEEE Trans. Ind. Electron.*, vol. 65, no. 2, pp. 1187–1195, Feb. 2018.
[8] H. Du, X. Chen, G. Wen, X. Yu, and J. Lü, "Discrete-time fast terminal sliding mode control for permanent magnet linear motor," *IEEE Trans. Ind. Electron.*, vol. 65, no. 12, pp. 9916–9927, Dec. 2018.
[9] Z. Zhang, H. Zhou, J. Duan, and B. Kou, "Research on permanent magnet linear synchronous motors with ring windings for electromagnetic launch system," *IEEE Trans. Plasma Sci.*, vol. 45, no. 7, pp. 1161–1167, Jul. 2017.

[10] R. Cao, M. Cheng, C. Mi, W. Hua, X. Wang, and W. Zhao, "Modeling of a complementary and modular linear flux-switching permanent magnet motor for urban rail transit applications," *IEEE Trans. Energy Convers.*, vol. 27, no. 2, pp. 489–497, Jun. 2012.

[11] W. Zhao, A. Yang, J. Ji, Q. Chen, and J. Zhu, "Modified flux linkage observer for sensorless direct thrust force control of linear vernier permanent magnet motor," *IEEE Trans. Power Electron.*, to be published. DOI: 10.1109/TPEL.2018.2879411.

[12] M. Zhao *et al.*, "Development and analysis of novel flux switching transverse flux permanent magnet linear machine," *IEEE Trans. Ind. Electron.*, vol. 66, no. 6, pp. 4923–4933, Jun. 2019.

[13] Q. Lu, Y. Yao, J. Shi, Y. Shen, X. Huang, and Y. Fang, "Design and performance investigation of novel linear switched flux PM machines," *IEEE Trans. Ind. Appl.*, vol. 53, no. 5, pp. 4590–4602, Sep./Oct. 2017.

[14] R. Cao, Y. Jin, Z. Zhang, and M. Cheng, "A new double-sided linear flux switching permanent magnet motor with yokeless mover for electromagnetic launch system," *IEEE Trans. Energy Convers.*, to be published. DOI: 10.1109/TEC.2018.2867625.

[15] W. Huang, W. Hua, F. Yin, F. Yu, and J. Qi, "Model predictive thrust force control of a linear flux-switching permanent magnet machine with voltage vectors selection and synthesis," *IEEE Trans. Ind. Electron.*, vol. 66, no. 6, pp. 4956–4967, Jun. 2019. DOI: 10.1109/TIE.2018.2835381.

[16] M. A. M. Cheema, J. E. Fletcher, M. Farshadnia, D. Xiao, and M. F. Rahman, "Combined speed and direct thrust force control of linear permanent-magnet synchronous motors with sensorless speed estimation using a sliding-mode control with integral action," *IEEE Trans. Ind. Electron.*, vol. 64, no. 5, pp. 3489–3501, May 2017.

[17] W. Zhao, B. Wu, Q. Chen, and J. Zhu, "Fault-tolerant direct thrust force control for a dual inverter fed open-end winding linear vernier permanent-magnet motor using improved SVPWM," *IEEE Trans. Ind. Electron.*, vol. 65, no. 9, pp. 7458–7467, Sep. 2018.

[18] H. Karimi, S. Vaez-Zadeh, and F. R. Salmasi, "Combined vector and direct thrust control of linear induction motors with end effect compensation," *IEEE Trans. Energy Convers.*, vol. 31, no. 1, pp. 196–205, Mar. 2016.

[19] C. Sung and Y. Huang, "Based on direct thrust control for linear synchronous motor systems," *IEEE Trans. Ind. Electron.*, vol. 56, no. 5, pp. 1629–1639, May 2009.

[20] W. Wang, M. Cheng, B. Zhang, Y. Zhu, and S. Ding, "A fault-tolerant permanent magnet traction module for subway application," *IEEE Trans. Power Electron.*, vol. 29, no. 4, pp. 1646–1658, Apr. 2014.

[21] S. C. Chang and S. N. Yeh, "Current sensorless field-oriented control of induction motors," *IEE Proc. – Elect. Power Appl.*, vol. 143, no. 6, pp. 492–500, Nov. 1996.

[22] S. Morimoto, M. Sanada, and Y. Takeda, "High-performance current-sensorless drive for PMSM and SynRM with only low-resolution position sensor," *IEEE Trans. Ind. Appl.*, vol. 39, no. 3, pp. 792–801, May/Jun. 2003.

[23] M. Zhao *et al.*, "Current sensorless MTPA operation of interior PMSM Drives for vehicular applications," *IEEE Trans. Ind. Electron.*, vol. 67, no. 8, pp. 6872–6881, Aug. 2018.

[24] S. K. Kommuri, S. B. Lee, and K. C. Veluvolu, "Robust sensor-fault-tolerance with sliding mode estimation and control for PMSM drives," *IEEE Trans. Mech.*, vol. 23, no. 1, pp. 17–28, Feb. 2018.

[25] K. Xiahou, X. Lin, Y. Liu, and Q. H. Wu, "Robust rotor-current sensorless control of doubly fed induction generators," *IEEE Trans. Energy Convers.*, vol. 33, no. 2, pp. 897–899, Jun. 2018.

[26] M. Bertoluzzo, G. Buja, and R. Menis, "Direct torque control of an induction motor using a single current sensor," *IEEE Trans. Ind. Electron.*, vol. 53, No. 3, pp. 778–784, Jun. 2006.

[27] W. Wang, M. Cheng, Z. Wang, and B. Zhang, "Fast switching direct torque control using a single DC-link current sensor," *J. Power Electron.*, vol. 12, no. 6, pp. 895–903, Nov. 2012.

[28] Y. Xu, H. Yan, J. Zou, B. Wang, and Y. Li, "Zero voltage vector sampling method for PMSM three-phase current reconstruction using single current sensor," *IEEE Trans. Power Electron.*, vol. 32, no. 5, pp. 3797–3807, May 2017.

[29] S. Song, Z. Xia, G. Fang, R. Ma, and W. Liu, "Phase current reconstruction and control of three-phase switched reluctance machine with modular power converter using single DC-link current sensor," *IEEE Trans. Power Electron.*, vol. 33, no. 10, pp. 8637–8649, Oct. 2018.

[30] J. Lu, Y. Hu, and J. Liu, "Analysis and compensation of sampling errors in TPFS IPMSM drives with single current sensor," *IEEE Trans. Ind. Electron.*, vol. 66, no. 5, pp. 3852–3855, May 2019. DOI: 10.1109/TIE.2018.2838114.

[31] F. Blaabjerg, J. K. Pedersen, U. Jaeger, and P. Thoegersen, "Single current sensor technique in the DC link of three-phase PWM-VS inverters: a review and a novel solution," *IEEE Trans. Ind. Appl.*, vol. 33, no. 5, pp. 1241–1253, Sep./Oct. 1997.

[32] S. C. Yang, "Saliency-based position estimation of permanent-magnet synchronous machines using square-wave voltage injection with a single current sensor," *IEEE Trans. Ind. Appl.*, vol. 51, no. 2, pp. 1561–1571, Mar./Apr. 2015.

[33] J. H. Im and R. Y. Kim, "Improved saliency-based position sensorless control of interior permanent-magnet synchronous machines with single DC-link current sensor using current prediction method," *IEEE Trans. Ind. Electron.*, vol. 65, no. 7, pp. 5335–5343, Jul. 2018.

[34] C. Chakraborty and V. Verma, "Speed and current sensor fault detection and isolation technique for induction motor drive using axes transformation," *IEEE Trans. Ind. Electron.*, vol. 62, no. 3, pp. 1943–1954, Mar. 2015.

[35] M. Manohar and S. Das, "Current sensor fault-tolerant control for direct torque control of induction motor drive using flux-linkage observer," *IEEE Trans. Ind. Inf.*, vol. 13, no. 6, pp. 2824–2833, Dec. 2017.

[36] Y. Yu, Y. Zhao, B. Wang, X. Huang, and D. Xu, "Current sensor fault diagnosis and tolerant control for VSI-based induction motor drives," *IEEE Trans. Power Electron.*, vol. 33, no. 5, pp. 4238–4248, May 2018.

[37] W. Wang, Y. Feng, W. Hua, M. Cheng, and J. Hang, "Non-symmetrical permanent-magnet linear motor traction systems for subway applications," in *Proc. 43rd Annu. Conf. IEEE Ind. Electron. Soc.*, Beijing, China, 2017, pp. 3676–3681.

[38] K. L. Zhou and D. W. Wang, "Relationship between space-vector modulation and three-phase carrier-based PWM: A comprehensive analysis," *IEEE Trans. Ind. Electron.*, vol. 49, no. 1, pp. 186–196, Feb. 2002.

Wei Wang (S'10–M'14) was born in Jiangsu, China. He received the B.Sc. degree in electrical engineering from the Nanjing University of Science & Technology, Nanjing, China, in 2008, and the Ph.D. degree in electrical engineering from Southeast University, Nanjing, China, in 2014, respectively.

Since 2014, he has been with Southeast University, where he is currently an Associate Professor with the School of Electrical Engineering. From October 2011 to October 2012, he got the scholarship from China Scholarship Council and was a joint Ph.D. student with University of Lille 1, Lille, France. He has authored or coauthored more than 30 technical papers. His research interests include motor drives and traction system for rail transit.

Yanan Feng was born in Anhui, China. He received the B.Sc. degree in electrical engineering from Anhui University of Technology, Maanshan, China, in 2016. He is currently working toward the M.Sc. degree in electrical engineering at Southeast University, Nanjing, China.

His current research interests include electromagnetic analysis and electrical machine drive of primary permanent magnet linear motor and traction system of rail transit.

Yan Shi was born in Jiangsu Province, China. He received the B.Sc. degree in electrical engineering from Soochow University, Suzhou, China, in 2016. He is currently working toward the M.Sc. degree in electrical engineering at Southeast University, Nanjing, China.

His current research interests include electric drives and multilevel converters.

Ming Cheng (M'01–SM'02–F'15) received the B.Sc. and M.Sc. degrees from the Department of Electrical Engineering, Southeast University, Nanjing, China, in 1982 and 1987, respectively, and the Ph.D. degree from the Department of Electrical and Electronic Engineering, University of Hong Kong, Hong Kong, in 2001.

Since 1987, he has been with Southeast University, where he is currently a Distinguished Professor with the School of Electrical Engineering and the Director with the Research Center for Wind Power Generation. From January to April 2011, he was a Visiting Professor with the Wisconsin Electric Machine and Power Electronics Consortium, University of Wisconsin, Madison, WI, USA. He has authored or coauthored more than 300 technical papers and four books, and is the holder of 70 patents in these areas. His teaching and research interests include electrical machines, motor drives for EV, and renewable energy generation.

Prof. Cheng is a Fellow of the Institution of Engineering and Technology. He has served as the Chair and an Organizing Committee Member for many international conferences. He is a Distinguished Lecturer of the IEEE Industry Applications Society for 2015/2016.

Wei Hua (SM'16) was born in Taizhou, China, in 1978. He received the B.Sc. and Ph.D. degrees in electrical engineering from Southeast University, Nanjing, China, in 2001 and 2007, respectively.

Since 2007, he has been with Southeast University, where he is currently a Professor with the School of Electrical Engineering. He has authored or coauthored more than 100 technical papers and is the holder of 44 patents in his areas of interest. His teaching and research interests include the design, analysis, and control of electrical machines.

Zheng Wang (S'05–M'09–SM'14) received the B.Eng. and M.Eng. degrees from Southeast University, Nanjing, China, in 2000 and 2003, respectively, and the Ph.D. degree from The University of Hong Kong, Hong Kong, in 2008.

From 2008 to 2009, he was a Postdoctoral Fellow with Ryerson University, Toronto, ON, Canada. He is currently a Full Professor with the School of Electrical Engineering, Southeast University, Nanjing, China. He has authored or coauthored more than 80 internationally refereed papers and four books in these areas. His research interests include electric drives, power electronics, and distributed generation.

Prof. Wang received several academic awards including IEEE PES Chapter Outstanding Engineer Award, Best Paper Award of International Conference on Electrical Machines and Systems, Best Session Paper Award of IEEE Annual Meeting of Industrial Electronics, and Nanjing Outstanding Paper Award of Natural Science.